Astrodynamics Vol. 5, No. 2, 121–137, 2021 https://doi.org/10.1007/s42064-020-0093-6

Spiral trajectories induced by radial thrust with applications to generalized sails

Marco Bassetto (✉), Alessandro A. Quarta, Giovanni Mengali, and Vittorio Cipolla

Department of Civil and Industrial Engineering, University of Pisa, Pisa I-56122, Italy

ABSTRACT

In this study, new analytical solutions to the equations of motion of a propelled spacecraft are investigated using a shape-based approach. There is an assumption that the spacecraft travels a two-dimensional spiral trajectory in which the orbital radius is proportional to an assigned power of the spacecraft angular coordinate. The exact solution to the equations of motion is obtained as a function of time in the case of a purely radial thrust, and the propulsive acceleration magnitude necessary for the spacecraft to track the prescribed spiral trajectory is found in a closed form. The analytical results are then specialized to the case of a generalized sail, that is, a propulsion system capable of providing an outward radial propulsive acceleration, the magnitude of which depends on a given power of the Sun-spacecraft distance. In particular, the conditions for an outward radial thrust and the required sail performance are quantified and thoroughly discussed. It is worth noting that these propulsion systems provide a purely radial thrust when their orientation is Sun-facing. This is an important advantage from an engineering point of view because, depending on the particular propulsion system, a Sun-facing attitude can be stable or obtainable in a passive way. A case study is finally presented, where the generalized sail is assumed to start the spiral trajectory from the Earth's heliocentric orbit. The main outcome is that the required sail performance is in principle achievable on the basis of many results available in the literature.

KEYWORDS

radial thrust
spiral trajectory
shape-based approach
analytical solution
generalized sail

Research Article

Received: 27 April 2020
Accepted: 19 August 2020

1 Introduction

Analytical solutions to the differential equations that govern the motion of an orbiting propelled spacecraft are available in few cases only [1–3]. Closed-form solutions represent a very useful tool in the preliminary phase of mission design as they significantly reduce the computational cost that would otherwise be required by the numerical propagation of spacecraft dynamics.

Analytical solutions to the equations of motion can be found by using two different approaches. The first possibility is to solve the equations of motion for an assigned thrust profile, such as the case of a spacecraft subjected to a constant radial or circumferential propulsive acceleration. This problem was first investigated by Tsien [4], who found an explicit and an approximate solution to the radial and the circumferential case, respectively. Since then, many other authors have discussed the constant radial thrust problem. Prussing and Coverstone-Carroll addressed the problem of determining the escape conditions and the amplitude of the spacecraft radial displacement (in the absence of an escape) by introducing the concept of potential energy well, but confining their analysis to the case of a circular parking orbit [5]. Later, Mengali and Quarta adopted the same approach in order to extend the previous results to the more general case of an elliptic parking orbit [6]. The explicit solution found by Battin in terms of elliptic integrals is also noteworthy [7], as well as the accurate approximations of the spacecraft trajectory and the flight time found by Quarta and Mengali in terms of a Fourier series [8]. Gonzalo and Bombardelli found alternative solutions that

✉ marco.bassetto@ing.unipi.it

Nomenclature

a	semimajor axis (km)
a_c	characteristic acceleration (mm/s^2)
$\boldsymbol{a}_r$	propulsive acceleration, with $a_r \triangleq \boldsymbol{a}_r \cdot \hat{\boldsymbol{r}}$ (mm/s^2)
$\{c_1, c_2\}$	constants of integration, see Eq. (12)
$\boldsymbol{e}$	eccentricity vector, with $e \triangleq \|\boldsymbol{e}\|$
h	specific angular momentum magnitude (km^2/s)
O	primary body center of mass
p	semilatus rectum (km)
r	orbital radius (km)
$\hat{\boldsymbol{r}}$	radial unit vector
$r_\oplus$	reference distance 1 au
S	spacecraft center of mass
t	time (year)
$\mathcal{T}$	polar reference frame
$\boldsymbol{v}$	spacecraft velocity vector (km/s)
v_r	radial component of $\boldsymbol{v}$ (km/s)
v_θ	transversal component of $\boldsymbol{v}$ (km/s)
α	dimensionless spiral parameter, see Eq. (6)
β	constant, see Eq. (61)
γ	dimensionless design parameter, see Eq. (38)
θ	polar angle (rad)
$\hat{\boldsymbol{\theta}}$	transversal unit vector
μ	gravitational parameter (km^3/s^2)
ν	spacecraft true anomaly (rad)
χ	dimensionless auxiliary function, see Eq. (14)
ω	argument of periapsis (rad)
Subscripts	
0	initial, parking orbit
max	maximum
$\oplus$	the Earth
$\odot$	the Sun
Superscripts	
$\cdot$	time derivative
$\sim$	threshold value
$\star$	optimal

involve asymptotic expansions [9], while Izzo and Biscani showed that a solution relating the state variables to a time parameter can be expressed in terms of Weierstrass elliptic and related functions [10].

After the pioneering work of Tsien [4], the constant circumferential thrust problem has also been an object of study. For example, Battin proposed an approximate solution under the assumptions of circular parking orbit, two-dimensional motion, and low thrust [7]. More recently, Quarta and Mengali proposed an analytical approximation of the spacecraft escape conditions and provided a simple expression for the escape distance [11], while Niccolai *et al.* [12] analyzed the two-dimensional dynamics of a spacecraft with a constant and circumferential low propulsive acceleration using the perturbative approach conceived by Bombardelli *et al.* [13]. Finally, Quarta *et al.* investigated the minimum-time trajectories from a circular parking orbit towards the apocenter of a rectilinear ellipse assuming that the spacecraft is subjected to a continuous circumferential thrust [14].

Benney was the first author to propose approximate solutions to the motion of a spacecraft subjected to a constant tangential thrust [15], while Boltz addressed the same problem assuming that the ratio of the thrust to the local gravitational pull is constant [16]. Finally, it is worth mentioning the work of Roa *et al.* [17], who presented a new analytical solution to the motion of a continuously accelerated spacecraft, wherein its thrust magnitude is assumed to decrease with the square of the spacecraft orbital radius. In particular, Roa *et al.* found

out that the dynamical system admits two integrals of motion resulting from the energy and angular momentum equations, and identified three subfamilies of spiral trajectories depending on the sign of a modified mechanical energy [17].

The second possibility to determine the analytical solutions to the equations of motion is represented by the shape-based approach. In this case, the thrust profile is derived such that a given trajectory may be followed by the spacecraft. For example, the possibility of generating a logarithmic spiral trajectory was first investigated by Bacon [18] and Tsu [19], the latter suggesting the use of solar sails [20–22]. In fact, a solar sail can travel along a logarithmic spiral with a constant attitude with respect to the Sun–spacecraft line, as thoroughly discussed by Bassetto *et al.* [23], who focused on the requirements to be met to place a spacecraft in a logarithmic spiral trajectory without any impulsive maneuver. Petropoulos and Longuski introduced an exponential sinusoid where four independent constants are used for describing the shape of the spacecraft trajectory [24]. In particular, Ref. [24] derived closed-form relations for the angular rate and the required tangential acceleration. Then, Izzo used the concept of the exponential sinusoid for solving the multi-revolution Lambert's problem [25], while Wall and Conway proposed fifth- and sixth-degree inverse polynomial functions that are capable of providing near-optimal solutions to many mission scenarios [26]. Finally, Taheri and Abdelkhalik developed a new flexible and effective method, suitable for the preliminary design of different scenarios, to approximate low-thrust trajectories using the finite Fourier series [27–29].

In the context of shape-based approaches, the aim of this paper is to analyze the generation of two-dimensional spiral trajectories in which the spacecraft orbital radius is proportional to a given power of its angular coordinate. There is an assumption that the spacecraft is subjected to a purely radial propulsive acceleration of adjustable magnitude during the entire transfer. It turns out that an exact solution to the equations of motion exists, allowing all of the spacecraft state variables and the orbital elements of the osculating orbit to be explicitly written as a function of time.

The general solution, which can be applied to any propulsion system that can provide a purely radial thrust, is specialized in a heliocentric framework to the class of the generalized sails [30–32]. This type of thrusters includes all the propellantless propulsion systems that provide an outward radial propulsive acceleration with a magnitude that scales as a certain power of the Sun–spacecraft distance. Electric solar wind sails (E-sails) [33–37], magnetic sails (magsails) [38–42], solar sails [20–22], and smart dusts (SDs) [43, 44] belong to this class of propulsion systems. Each of them exploits a peculiar form of energy coming from the Sun. In particular, E-sails and magsails extract momentum from the charged particles constituting the solar wind by using an artificial electric and magnetic field, respectively. Differently, solar sails and SDs take advantage of solar radiation pressure, which acts on a membrane made of reflective material, thus generating a propulsive acceleration. It is worth noting that these propulsion systems provide a purely radial thrust when their orientation is Sun–facing, that is, when the sail nominal plane is orthogonal to the propagation direction of photons or solar wind particles. From an engineering point of view, this is a significant advantage because such an attitude is easy to maintain in most cases. For example, a Sun–facing attitude is shown to be stable when using an E-sail [45], while SDs are able to passively obtain a Sun–facing orientation thanks to an appropriate system architecture (which is composed of a single plate with many surface etches called "facets") that exploits solar radiation torques [46].

E-sail- and solar sail-based trajectories have already been analyzed in an attempt to find approximate analytical solutions to the equations of motion. For example, Quarta and Mengali proposed an analytical approximation for the trajectory of a low-performance E-sail with a constant thrust angle [47]. In a subsequent work [48], Quarta and Mengali offered an approximate expression of the E-sail heliocentric trajectory by reducing the problem to the dynamics of an equivalent nonlinear oscillator with a single degree of freedom, and assuming that the E-sail provides a purely outward radial thrust. Moreover, Niccolai *et al.* analyzed the two-dimensional heliocentric dynamics of an E-sail with a fixed attitude, and found an approximate solution to the equations of motion through the use of an asymptotic expansion procedure [49]. In the field of solar sails, Quarta and Mengali investigated approximate solutions to circle-to-circle orbit transfers [50], and Niccolai *et al.* analyzed solar sail trajectories with an asymptotic expansion method [51], while Caruso *et al.* presented a procedure to generate an approximate optimal trajectory through a finite Fourier series [52].

In this study, the characteristic acceleration necessary for the generalized sail to track the desired heliocentric spiral trajectory is found analytically. The characteristic acceleration, which is a sail performance parameter, is here defined as the magnitude of the radial propulsive acceleration at the reference distance of one astronomical unit from the Sun. A continuous modulation of the characteristic acceleration is actually feasible for all the aforementioned sails. For example, the characteristic acceleration of an E-sail may be controlled by modulating the tether electrical voltage [45]. For a solar sail, such a control may be achieved by partially or totally refolding the reflective film, by rotating parts of it, or by varying the sail orientation over time to obtain a modulated thrust that, on average, is purely radial [3, 53]. Another option for controlling the characteristic acceleration of a solar sail is to cover its reflective film with electrochromic materials [54], which can change their reflectivity coefficient through the application of an electrical voltage. The same strategy is commonly used for millimeter-scale solar sails and SDs [43, 44]. Finally, the characteristic acceleration of a Magsail can be adjusted, in principle, by varying the electrical current flowing in its ring [40, 41].

The remainder of this paper is organized as follows. Section 2 deals with the trajectory analysis and presents the analytical solution to the equations of motion assuming a purely radial thrust and a direct proportionality between the spacecraft orbital radius and a given power of its angular coordinate. The magnitude of the propulsive acceleration that is required for the spacecraft to track the prescribed spiral trajectory is also derived in Section 2. Section 3 investigates the possibility of generating heliocentric spiral trajectories using a generalized sail and quantifies the conditions for an outward radial thrust and the required sail performance. Section 4 discusses a case study assuming that the sail enters the spiral trajectory starting from the Earth's heliocentric orbit. Finally, Section 5 presents the concluding remarks.

2 Trajectory analysis

With reference to Fig. 1, consider a spacecraft S that initially covers a Keplerian parking orbit around a primary body O of gravitational parameter μ, and introduce a polar reference frame $\mathcal{T}(O;\hat{\boldsymbol{r}},\hat{\boldsymbol{\theta}})$ with origin at O, where $\hat{\boldsymbol{r}}$ and $\hat{\boldsymbol{\theta}}$ are the radial and transversal unit vectors, respectively. The spacecraft position is described by the orbital radius r (i.e., the primary-spacecraft distance) and by the polar angle θ, the latter being measured counterclockwise on the parking orbit plane from a fixed direction. Besides, let $v_r \triangleq \boldsymbol{v}\cdot\hat{\boldsymbol{r}}$ and $v_\theta \triangleq \boldsymbol{v}\cdot\hat{\boldsymbol{\theta}}$ be the two components of the spacecraft velocity vector $\boldsymbol{v}$; see Fig. 1. At the initial time $t = t_0 \triangleq 0$, the spacecraft angular position is $\theta_0 \triangleq \theta(t_0)$, the orbital radius is $r_0 \triangleq r(t_0)$, and the two components of the spacecraft velocity are $v_{r_0} \triangleq v_r(t_0)$ and $v_{\theta_0} \triangleq v_\theta(t_0)$.

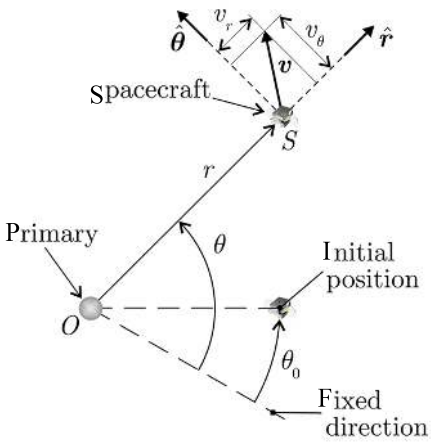

Fig. 1 Polar reference frame and spacecraft state variables.

The spacecraft is equipped with a continuous-thrust propulsion system that provides a purely radial propulsive acceleration $\boldsymbol{a}_r = a_r\hat{\boldsymbol{r}}$ of adjustable magnitude $|a_r|$. As $\boldsymbol{a}_r\cdot\hat{\boldsymbol{\theta}} = 0$, the specific angular momentum $h \triangleq rv_\theta$ is a constant of motion, and the transversal component of the velocity vector may be written as $v_\theta = r_0 v_{\theta_0}/r$. Hence, the spacecraft dynamics is described by the following system of nonlinear differential equations:

$$\dot{r} = v_r \tag{1}$$

$$\dot{\theta} = \frac{r_0 v_{\theta_0}}{r^2} \tag{2}$$

$$\dot{v}_r = -\frac{\mu}{r^2} + \frac{r_0^2 v_{\theta_0}^2}{r^3} + a_r \tag{3}$$

$$\dot{v}_\theta = -\frac{r_0 v_{\theta_0} v_r}{r^2} \tag{4}$$

with initial conditions

$$r(t_0) = r_0, \theta(t_0) = \theta_0, v_r(t_0) = v_{r_0}, v_\theta(t_0) = v_{\theta_0} \tag{5}$$

There is an assumption that the spacecraft is able to exactly track a generic spiral trajectory in the form

$$r = r_0\left(\frac{\theta}{\theta_0}\right)^\alpha \tag{6}$$

provided that the radial thrust magnitude may be suit-

ably modulated. In Eq. (6), $\alpha \in \mathbb{R}_{\neq 0}$ is a dimensionless parameter that characterizes the type of spiral. Typical examples are obtained with $\alpha = -1$ (the hyperbolic spiral), $\alpha = -1/2$ (the lituus), $\alpha = 1/2$ (the Fermat's spiral), and $\alpha = 1$ (the Archimedean spiral). Note that, when the trajectory is in the form of Eq. (6), the spacecraft radial velocity v_r is constrained to the transversal velocity v_θ. In fact, according to Eq. (6), the time derivative of r can be written in a compact form as

$$\dot{r} = \frac{\alpha r \dot{\theta}}{\theta} \tag{7}$$

Bearing in mind that $v_r = \dot{r}$ and $v_\theta = r\dot{\theta}$, Eqs. (6) and (7) provide

$$\frac{v_r}{v_\theta} = \frac{\alpha}{\theta} \tag{8}$$

so that the initial conditions in Eq. (5) must be selected to satisfy the constraint

$$v_{r_0} = \frac{\alpha v_{\theta_0}}{\theta_0} \tag{9}$$

The time evolution of the spacecraft state variables $\{r, \theta, v_r, v_\theta\}$ can now be found. To that end, first consider the time variation of the polar angle $\theta \triangleq \theta(t)$, which may be obtained by substituting Eq. (6) into Eq. (2) to get the following first order differential equation:

$$\dot{\theta} = \frac{\alpha^{2\alpha} v_{\theta_0}^{2\alpha+1}}{r_0 v_{r_0}^{2\alpha}} \theta^{-2\alpha} \tag{10}$$

which can be solved by separation of variables. The result is

$$\theta = \begin{cases} c_2[c_1 + (1+2\alpha)t]^{\frac{1}{1+2\alpha}}, & \text{if } \alpha \neq \{-1/2, 0\} \\ c_2 \exp(c_1 t), & \text{if } \alpha = -1/2 \end{cases} \tag{11}$$

where $\{c_1, c_2\}$ are two constants of integration, given by

$$c_1 = \begin{cases} \dfrac{\alpha r_0}{v_{r_0}}, & \text{if } \alpha \neq \{-1/2, 0\} \\ -\dfrac{2v_{r_0}}{r_0}, & \text{if } \alpha = -1/2 \end{cases}$$

$$c_2 = \begin{cases} \dfrac{v_{\theta_0}}{r_0}\left(\dfrac{\alpha r_0}{v_{r_0}}\right)^{\frac{2\alpha}{1+2\alpha}}, & \text{if } \alpha \neq \{-1/2, 0\} \\ -\dfrac{v_{\theta_0}}{2v_{r_0}}, & \text{if } \alpha = -1/2 \end{cases} \tag{12}$$

The two cases of $\alpha \neq \{-1/2, 0\}$ and $\alpha = -1/2$ are now analyzed separately.

2.1 Case of $\alpha \neq \{-1/2, 0\}$

In this scenario, rearranging Eqs. (11) and (12), the time variation of the spacecraft polar angle can be rewritten as

$$\theta = \frac{\alpha v_{\theta_0}}{v_{r_0}} \chi^{\frac{1}{1+2\alpha}} \tag{13}$$

where

$$\chi \triangleq 1 + \frac{(1+2\alpha) v_{r_0} t}{\alpha r_0} \tag{14}$$

is a dimensionless auxiliary function of time. Substituting Eq. (13) into Eq. (6), the χ-variation of the primary-spacecraft distance becomes

$$r = r_0 \chi^{\frac{\alpha}{1+2\alpha}} \tag{15}$$

while, with the aid of Eqs. (7) and (10), the two components of the spacecraft velocity vector are

$$v_r = v_{r_0} \chi^{-\frac{1+\alpha}{1+2\alpha}}, \quad v_\theta = v_{\theta_0} \chi^{-\frac{\alpha}{1+2\alpha}} \tag{16}$$

Equation (15) provides a positive value of r as long as $(1+2\alpha)v_{r_0}/\alpha > 0$. When, instead, $(1+2\alpha)v_{r_0}/\alpha < 0$, the physical constraint $r > 0$ is met provided that

$$t < t_{\max} \triangleq -\frac{\alpha r_0}{(1+2\alpha) v_{r_0}} \tag{17}$$

Finally, note that, when $v_{r_0} > 0$, $r \to +\infty$ as $t \to +\infty$ (or $t \to t_{\max}$) if $\alpha < -1/2$ or $\alpha > 0$ (or $-1/2 < \alpha < 0$). Conversely, $r \to 0$ as $t \to t_{\max}$ (or $t \to +\infty$) if $\alpha < -1/2$ or $\alpha > 0$ (or $-1/2 < \alpha < 0$).

The closed-form expressions of the state variables allow the orbital elements $\{a, e, \omega, \nu\}$ of the osculating orbit to be analytically determined as a function of time. To that end, consider the eccentricity vector $\boldsymbol{e}$, defined as

$$\boldsymbol{e} \triangleq e_r \hat{\boldsymbol{r}} + e_\theta \hat{\boldsymbol{\theta}} = \frac{p - r}{r} \hat{\boldsymbol{r}} - \frac{r v_r v_\theta}{\mu} \hat{\boldsymbol{\theta}} \tag{18}$$

where $p \equiv p_0 \triangleq r_0^2 v_{\theta_0}^2 / \mu$ is the (constant) semilatus rectum of the spacecraft osculating orbit. From Eqs. (15) and (16), the radial and transversal components of $\boldsymbol{e}$ may be explicitly written as

$$e_r = \frac{r_0 v_{\theta_0}^2}{\mu} \chi^{-\frac{\alpha}{1+2\alpha}} - 1 \tag{19}$$

$$e_\theta = -\frac{r_0 v_{r_0} v_{\theta_0}}{\mu} \chi^{-\frac{1+\alpha}{1+2\alpha}} \tag{20}$$

Accordingly, the eccentricity e of the spacecraft osculating orbit is

$$e = \|\boldsymbol{e}\| = \sqrt{\frac{r_0^2 v_{\theta_0}^4}{\mu^2} \chi^{-\frac{2\alpha}{1+2\alpha}} - \frac{2 r_0 v_{\theta_0}^2}{\mu} \chi^{-\frac{\alpha}{1+2\alpha}} + 1 + \frac{r_0^2 v_{r_0}^2 v_{\theta_0}^2}{\mu^2} \chi^{-\frac{2+2\alpha}{1+2\alpha}}} \tag{21}$$

whereas the semimajor axis a is

$$a = \frac{p_0}{1-e^2} = \frac{\mu r_0}{2\mu\chi^{-\frac{\alpha}{1+2\alpha}} - r_0 v_{\theta_0}^2 \chi^{-\frac{2\alpha}{1+2\alpha}} - r_0 v_{r_0}^2 \chi^{-\frac{2+2\alpha}{1+2\alpha}}} \tag{22}$$

Because the argument of periapsis is here defined as the angle between the initial primary-spacecraft line and the direction of $\boldsymbol{e}$ (see Fig. 2), the expression of $\omega \in [0, 2\pi)$ rad is

$$\omega = \frac{\alpha v_{\theta_0}}{v_{r_0}}(\chi^{\frac{1}{1+2\alpha}} - 1) + \arctan\left(\frac{-\frac{v_{r_0}}{v_{\theta_0}}\chi^{-\frac{1+\alpha}{1+2\alpha}}}{\chi^{-\frac{\alpha}{1+2\alpha}} - \frac{\mu}{r_0 v_{\theta_0}^2}}\right) \tag{23}$$

Finally, the spacecraft true anomaly $\nu \in [0, 2\pi)$ rad along the osculating orbit is

$$\nu = -\arctan\left(\frac{-\frac{v_{r_0}}{v_{\theta_0}}\chi^{-\frac{1+\alpha}{1+2\alpha}}}{\chi^{-\frac{\alpha}{1+2\alpha}} - \frac{\mu}{r_0 v_{\theta_0}^2}}\right) \tag{24}$$

2.2 Case of $\alpha = -1/2$

In this case, using again Eqs. (11) and (12), the function $\theta \triangleq \theta(t)$ can be written as

$$\theta = -\frac{v_{\theta_0}}{2v_{r_0}} \exp\left(-\frac{2v_{r_0}t}{r_0}\right) \tag{25}$$

Substituting Eq. (25) into Eq. (6) provides the time variation of the orbital radius, viz.

$$r = r_0 \exp\left(\frac{v_{r_0}t}{r_0}\right) \tag{26}$$

with $r > 0$ for any $t \geqslant t_0$. Note that now $r \to +\infty$ (or $r \to 0$) when $v_{r_0} > 0$ (or $v_{r_0} < 0$) as $t \to +\infty$. Moreover, the two components of the spacecraft velocity vector are

$$v_r = v_{r_0} \exp\left(\frac{v_{r_0}t}{r_0}\right), v_\theta = v_{\theta_0} \exp\left(-\frac{v_{r_0}t}{r_0}\right) \tag{27}$$

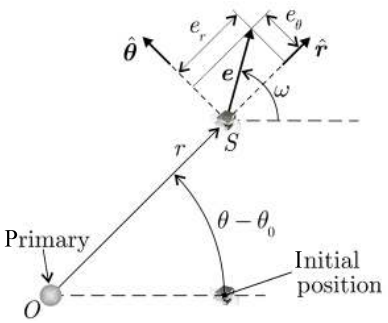

Fig. 2 Eccentricity vector components and angle ω.

while the radial and transversal components of $\boldsymbol{e}$ are

$$e_r = \frac{r_0 v_{\theta_0}^2}{\mu} \exp\left(-\frac{v_{r_0}t}{r_0}\right) - 1 \tag{28}$$

$$e_\theta = -\frac{r_0 v_{r_0} v_{\theta_0}}{\mu} \exp\left(\frac{v_{r_0}t}{r_0}\right) \tag{29}$$

Accordingly, the osculating orbit eccentricity e is

$$e = \sqrt{\begin{array}{l}\dfrac{r_0^2 v_{\theta_0}^4}{\mu^2} \exp\left(-\dfrac{2v_{r_0}t}{r_0}\right) - \dfrac{2r_0 v_{\theta_0}^2}{\mu} \exp\left(-\dfrac{v_{r_0}t}{r_0}\right) \\ +1 + \dfrac{r_0^2 v_{r_0}^2 v_{\theta_0}^2}{\mu^2} \exp\left(\dfrac{2v_{r_0}t}{r_0}\right)\end{array}} \tag{30}$$

whereas the semimajor axis a becomes

$$a = \frac{\mu r_0}{\begin{array}{l}2\mu \exp\left(-\dfrac{v_{r_0}t}{r_0}\right) - r_0 v_{\theta_0}^2 \exp\left(-\dfrac{2v_{r_0}t}{r_0}\right) \\ -r_0 v_{r_0}^2 \exp\left(\dfrac{2v_{r_0}t}{r_0}\right)\end{array}} \tag{31}$$

Finally, the angle ω is given by

$$\omega = \frac{v_{\theta_0}}{2v_{r_0}}\left[1 - \exp\left(-\frac{2v_{r_0}t}{r_0}\right)\right] + \arctan\left[\frac{-\frac{v_{r_0}}{v_{\theta_0}} \exp\left(\frac{v_{r_0}t}{r_0}\right)}{\exp\left(-\frac{v_{r_0}t}{r_0}\right) - \frac{\mu}{r_0 v_{\theta_0}^2}}\right] \tag{32}$$

while the spacecraft true anomaly ν along the osculating orbit is

$$\nu(t) = -\arctan\left[\frac{-\frac{v_{r_0}}{v_{\theta_0}} \exp\left(\frac{v_{r_0}t}{r_0}\right)}{\exp\left(-\frac{v_{r_0}t}{r_0}\right) - \frac{\mu}{r_0 v_{\theta_0}^2}}\right] \tag{33}$$

2.3 Required propulsive acceleration

Having shown that a spiral trajectory in the form of Eq. (6) is actually a particular solution to the equations of motion of a radially propelled spacecraft, the required propulsive acceleration can now be calculated. To that end, recall that a_r must satisfy Eq. (3) at any time $t \geqslant t_0$. Substituting Eqs. (1) and (2) into Eq. (3) yields

$$a_r = \alpha r_0 \frac{\theta^{\alpha-2}}{\theta_0^\alpha}[\theta\ddot{\theta} + (\alpha - 1)\dot{\theta}^2] - r_0\dot{\theta}^2\left(\frac{\theta}{\theta_0}\right)^\alpha + \frac{\mu}{r_0^2}\left(\frac{\theta_0}{\theta}\right)^{2\alpha} \tag{34}$$

where $\{\dot{\theta}, \ddot{\theta}\}$ are obtained from Eqs. (13) and (25) as

$$\dot{\theta} = \begin{cases} \dfrac{v_{\theta_0}}{r_0}\chi^{-\frac{2\alpha}{1+2\alpha}} & \text{if } \alpha \neq \{-1/2, 0\} \\ \dfrac{v_{\theta_0}}{r_0}\exp\left(-\dfrac{2v_{r_0}t}{r_0}\right) & \text{if } \alpha = -1/2 \end{cases} \tag{35}$$

$$\ddot{\theta} = \begin{cases} -\dfrac{2v_{r_0}v_{\theta_0}}{r_0^2}\chi^{-\frac{1+4\alpha}{1+2\alpha}} & \text{if } \alpha \neq \{-1/2, 0\} \\ -\dfrac{2v_{r_0}v_{\theta_0}}{r_0^2}\exp\left(-\dfrac{2v_{r_0}t}{r_0}\right) & \text{if } \alpha = -1/2 \end{cases} \tag{36}$$

Accordingly, Eq. (34) can be rewritten using Eqs. (13), (25), (35), (36) to obtain the expression of $a_r \triangleq a_r(t)$ as a function of $\{\alpha, r_0, v_{r_0}, v_{\theta_0}\}$, viz.

$$a_r = \begin{cases} -\dfrac{1+\alpha}{\alpha}\dfrac{v_{r_0}^2}{r_0}\chi^{-\frac{2+3\alpha}{1+2\alpha}} - \dfrac{v_{\theta_0}^2}{r_0}\chi^{-\frac{3\alpha}{1+2\alpha}} + \dfrac{\mu}{r_0^2}\chi^{-\frac{2\alpha}{1+2\alpha}}, \\ \qquad\qquad \text{if } \alpha \neq \{-1/2, 0\} \\ \dfrac{v_{r_0}^2}{r_0}\exp\left(\frac{v_{r_0}t}{r_0}\right)\left[1 - \dfrac{v_{\theta_0}^2}{v_{r_0}^2}\exp\left(-\dfrac{4v_{r_0}t}{r_0}\right)\right] \\ +\dfrac{\mu}{r_0^2}\exp\left(-\dfrac{2v_{r_0}t}{r_0}\right), \qquad \text{if } \alpha = -1/2 \end{cases} \tag{37}$$

Equation (37) provides the spacecraft propulsive acceleration that is required to travel an assigned spiral trajectory with $r \propto \theta^\alpha$. The next section analyzes the problem of creating a generic spiral trajectory using a generalized sail-based spacecraft [30–32].

3 Generalized sail-based spiral trajectories

The results obtained so far are general because they may be applied to any propulsive system that is able to provide a purely radial thrust. An interesting class of propulsion systems that may be employed for generating spiral trajectories is offered by the generalized sails [30–32]. The concept of generalized sail is useful for describing, in a heliocentric mission scenario, the propulsive acceleration of a propellantless propulsion system when the thrust vector is oriented along the outward radial direction and its magnitude depends on a given power of the Sun–spacecraft distance r. Precisely, the expression of $\boldsymbol{a}_r \cdot \hat{\boldsymbol{r}}$ for a generalized is

$$\boldsymbol{a}_r \cdot \hat{\boldsymbol{r}} = a_{\mathrm{c}}\left(\frac{r_\oplus}{r}\right)^\gamma \tag{38}$$

where $r_\oplus \triangleq 1$ au is a reference distance, $a_{\mathrm{c}} \geqslant 0$ is the spacecraft characteristic acceleration (that is, the value of $\boldsymbol{a}_r \cdot \hat{\boldsymbol{r}}$ at a Sun–spacecraft distance equal to $r_\oplus$), and $\gamma \geqslant 0$ is a dimensionless design parameter that defines the type of propulsion system. For example, a value of $\gamma = 1$ models an E-sail [45, 55], $\gamma = 4/3$ describes the heliocentric behavior of a magsail with a large loop radius [56, 57], while $\gamma = 2$ is consistent with the thrust model of a solar sail [20] or a magsail with a huge loop radius [56, 57].

In order to make the generalized sail-based spacecraft capable of following the assigned spiral trajectory, the radial propulsive acceleration of Eq. (38) must comply with the required value of Eq. (37). To that end, it is useful to rewrite Eq. (37) so that the dependence of a_r on the Sun–spacecraft distance r is made explicit, viz.

$$a_r = -\frac{(1+\alpha)v_{r_0}^2 r_0^{\frac{2+2\alpha}{\alpha}}}{\alpha r^{\frac{2+3\alpha}{\alpha}}} + \frac{\mu_\odot}{r^2} - \frac{r_0^2 v_{\theta_0}^2}{r^3} \tag{39}$$

where $\mu_\odot$ is the Sun's gravitational parameter. Note that Eq. (39) is valid for any $\alpha \neq 0$ and, therefore, it also includes the special case of $\alpha = -1/2$. From Eqs. (38) and (39), the required characteristic acceleration a_{c} can now be written as a function of r as

$$a_{\mathrm{c}} = -\frac{(1+\alpha)v_{r_0}^2 r_0^{\frac{2+2\alpha}{\alpha}}}{\alpha r_\oplus^\gamma r^{\frac{2+3\alpha-\alpha\gamma}{\alpha}}} + \frac{\mu_\odot}{r_\oplus^\gamma r^{2-\gamma}} - \frac{r_0^2 v_{\theta_0}^2}{r_\oplus^\gamma r^{3-\gamma}} \tag{40}$$

The characteristic acceleration of a generalized sail must therefore be adjusted with continuity according to Eq. (40) to maintain the spacecraft along the assigned spiral trajectory of parameters $\{\alpha, r_0, v_{r_0}, v_{\theta_0}\}$.

3.1 Condition for a generalized sail outward radial thrust

A generalized sail can only generate an outward propulsive acceleration, which amounts to stating that its characteristic acceleration must be non-negative. For a given value of α that defines the spiral type, it is therefore necessary to investigate the conditions under which $a_{\mathrm{c}} \geqslant 0$ for $t \geqslant t_0$.

First, consider the value of a_{c} when $r = r_0$. From Eq. (40), one has

$$a_{\mathrm{c}_0} \triangleq a_{\mathrm{c}}(r_0) = -\frac{(1+\alpha)v_{r_0}^2 r_0^{\gamma-1}}{\alpha r_\oplus^\gamma} + \frac{\mu_\odot r_0^{\gamma-2}}{r_\oplus^\gamma} - \frac{r_0^{\gamma-1}v_{\theta_0}^2}{r_\oplus^\gamma} \tag{41}$$

which is positive when

$$v_{\theta_0} < \widetilde{v}_{\theta_0} \triangleq \sqrt{\frac{\mu_\odot}{r_0} - \frac{(1+\alpha)v_{r_0}^2}{\alpha}} \tag{42}$$

while it is equal to zero when $v_{\theta_0} = \widetilde{v}_{\theta_0}$. In particular, when $\alpha < -1$ or $\alpha > 0$, the inequality of Eq. (42) exists only if $|v_{r_0}| \leqslant \sqrt{(1+\alpha)\mu_\odot/(\alpha r_0)}$. Figure 3 shows the maximum values of v_{θ_0} that ensure a non-negative value of a_{c_0}. The contour lines in Fig. 3 are reported in the plane (v_{r_0}, r_0) for $\alpha = \{-1, -1/2, 1/2, 1\}$, that is, for a hyperbolic spiral, a lituus, a Fermat's (or parabolic) spiral, and an Archimedean (or arithmetic) spiral, respectively. Note that, when $\alpha = -1$, the initial transversal velocity component must be less than $\sqrt{\mu_\odot/r_0}$, regardless of v_{r_0}; see Eq. (42) and Fig. 3(a). Instead, when $\alpha = -1/2$, the value of $\widetilde{v}_{\theta_0}$ is greater than v_{r_0} for any r_0; see Fig. 3(b). Finally, the grey areas in Figs. 3(c) and 3(d) correspond to the loci in which $|v_{r_0}| > \sqrt{(1+\alpha)\mu_\odot/(\alpha r_0)}$.

Equation (41) allows the designer to find the initial orbital parameters such that $a_{c_0} = 0$. To that end, the initial radial velocity component may be written as

$$v_{r_0} = \sqrt{\frac{\mu_\odot}{p_0}} e_0 \sin\nu_0 \tag{43}$$

where $e_0 \triangleq e(t_0)$ is the parking orbit eccentricity and $\nu_0 \triangleq \nu(t_0)$ is the initial spacecraft true anomaly. Substitute Eq. (43) into Eq. (42) to obtain

$$\widetilde{v}_{\theta_0} = \sqrt{\frac{\mu_\odot}{p_0}} \sqrt{1 + e_0\cos\nu_0 - \left(\frac{1+\alpha}{\alpha}\right) e_0^2 \sin^2\nu_0} \tag{44}$$

from which the tangent of the flight path angle when $a_{c_0} = 0$ is found as

$$\frac{e_0 \sin\nu_0}{1 + e_0\cos\nu_0} = \frac{v_{r_0}}{\widetilde{v}_{\theta_0}}$$

$$\equiv \frac{e_0 \sin\nu_0}{\sqrt{1 + e_0\cos\nu_0 - \left(\frac{1+\alpha}{\alpha}\right) e_0^2 \sin^2\nu_0}} \tag{45}$$

Assuming $e_0 \in (0, 1]$, Eq. (45) can now be solved with respect to $\cos\nu_0$, and the result is

$$\cos\nu_0 = \frac{\alpha - \text{sign}(\alpha)\sqrt{\alpha^2 + 4e_0^2(1+\alpha)}}{2e_0} \tag{46}$$

where sign $(\square)$ is the signum function. When $e_0 > 1$ (hyperbolic parking orbit), Eq. (45) provides

$$\cos\nu_0 = \begin{cases} \dfrac{\alpha \pm \sqrt{\alpha^2 + 4e_0^2(1+\alpha)}}{2e_0}, \\ \qquad \text{if } -2e_0(e_0 - \sqrt{e_0^2 - 1}) < \alpha < -1 \\ \dfrac{\alpha + \sqrt{\alpha^2 + 4e_0^2(1+\alpha)}}{2e_0}, \qquad \text{if } -1 \leqslant \alpha < 0 \end{cases} \tag{47}$$

which implies that no solutions exist if $\alpha \leqslant -2e_0(e_0 - \sqrt{e_0^2 - 1})$ or $\alpha > 0$.

When investigating generalized sail-based spiral trajectories, it is reasonable to confine the analysis to the case of outward heliocentric spirals. In fact, an inward spiral would entail a negative value of a_c in some parts of the propelled trajectory and, as such, it could not be followed by a generalized sail. The following analysis is also limited to the case of elliptic parking orbits.

Assume now that the spacecraft starts a heliocentric spiral when $a_{c_0} = 0$. According to Eq. (46), the spacecraft initial true anomaly is given by

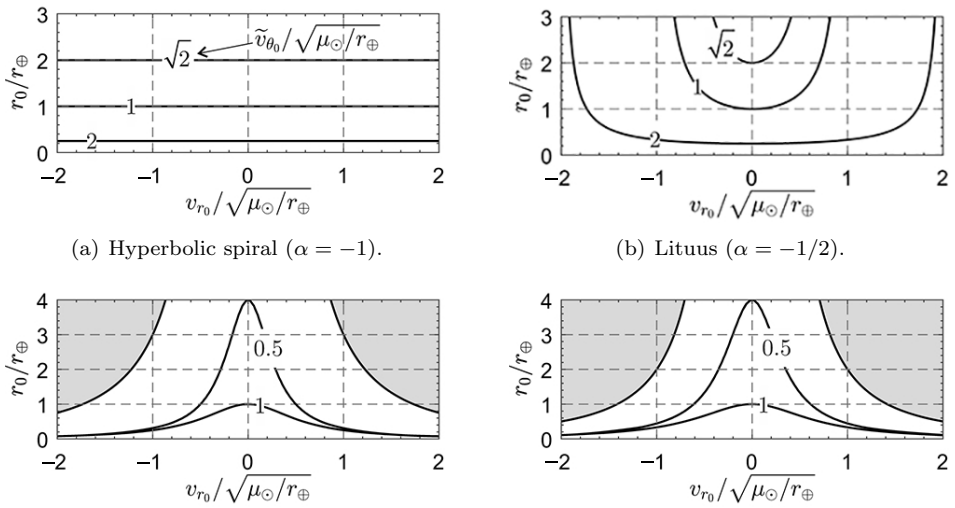

(a) Hyperbolic spiral ($\alpha = -1$).

(b) Lituus ($\alpha = -1/2$).

(c) Fermat's spiral ($\alpha = 1/2$).

(d) Archimedean spiral ($\alpha = 1$).

Fig. 3 Variation of $\widetilde{v}_{\theta_0}$ with $\{v_{r_0}, r_0\}$ for $\alpha = \pm\{1/2, 1\}$.

$$\nu_0 = \widetilde{\nu}_0 \triangleq \arccos\left[\frac{\alpha - \text{sign}\,(\alpha)\sqrt{\alpha^2 + 4e_0^2(1+\alpha)}}{2e_0}\right] \tag{48}$$

Note that $a_{c_0} < 0$ when $\nu_0 \in (0, \widetilde{\nu}_0)$, while $a_{c_0} > 0$ when $\nu_0 \in (\widetilde{\nu}_0, \pi\,\text{rad})$. For example, Fig. 4 shows the variation of $\widetilde{\nu}_0$ with α for $e_0 = \{0.1, 0.2, 0.3\}$. In particular, $\widetilde{\nu}_0 < \pi/2$ rad if $\alpha \in (-1, 0)$, $\widetilde{\nu}_0 = \pi/2$ rad if $\alpha = -1$, while $\widetilde{\nu}_0 > \pi/2$ rad if $\alpha < -1$ or $\alpha > 0$.

When $\nu_0 = \widetilde{\nu}_0$, the value of a_c is non-negative along the generic spiral when

$$\frac{(1+\alpha)v_{r_0}^2 r_0}{\alpha\mu_\odot}\left[1 - \left(\frac{r_0}{r}\right)^{2/\alpha}\right] + \frac{r}{r_0} - 1 \geqslant 0 \tag{49}$$

where, bearing in mind Eq. (48), $v_{r_0}^2$ and r_0 are given by

$$v_{r_0}^2 = \frac{\mu_\odot}{p_0}\left[e_0^2 - \frac{(p_0 - r_0)^2}{r_0^2}\right] \tag{50}$$

$$r_0 = \frac{2p_0}{\alpha - \text{sign}\,(\alpha)\sqrt{\alpha^2 + 4e_0^2(1+\alpha)} + 2} \tag{51}$$

Equation (49) is met for any $r \geqslant r_0$ when $\alpha \leqslant -2$ or $\alpha \geqslant -1$. If, instead, $\alpha \in (-2, -1)$, Eq. (49) is valid as long as the orbital radius is less than a threshold value, beyond which the value of the required characteristic acceleration becomes negative.

In other terms, when $\alpha \in (-2, -1)$, the required characteristic acceleration increases until a maximum is reached, after which it starts decreasing and eventually takes negative values. The value of r at which a_c becomes negative depends on α and on the parking orbit characteristics, as shown in Fig. 5 for $e_0 = \{0.1, 0.2, 0.3\}$. In particular, the grey areas in Fig. 5 correspond to the combinations of α and r when $a_c < 0$, while the contour lines represent the condition $a_c = 0$.

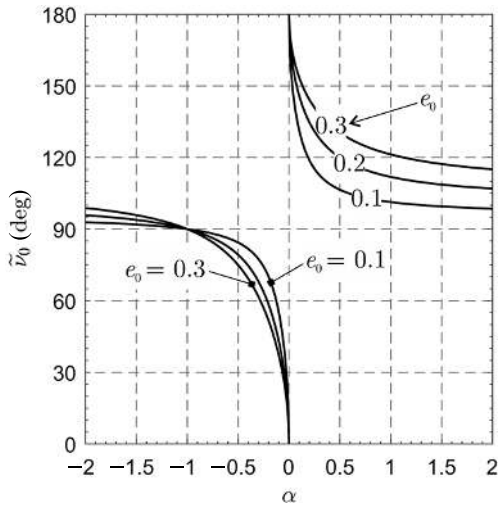

Fig. 4 Variation of $\widetilde{\nu}_0$ with α for $e_0 = \{0.1, 0.2, 0.3\}$.

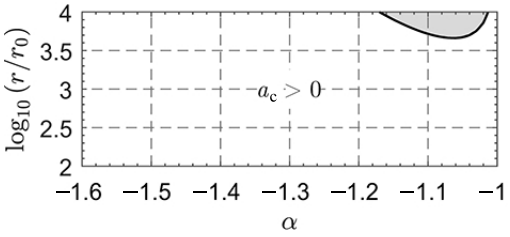

(a) $e_0 = 0.1$.

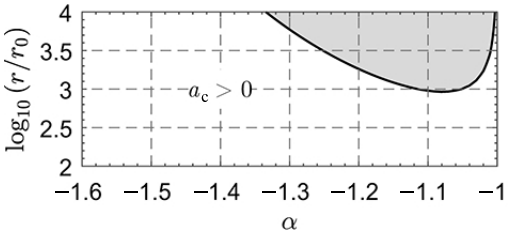

(b) $e_0 = 0.2$.

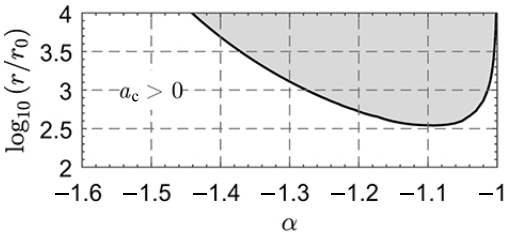

(c) $e_0 = 0.3$.

Fig. 5 Sign of a_c as a function of $\{\alpha, r\}$ when $a_{c_0} = 0$ and $e_0 = \{0.1, 0.2, 0.3\}$.

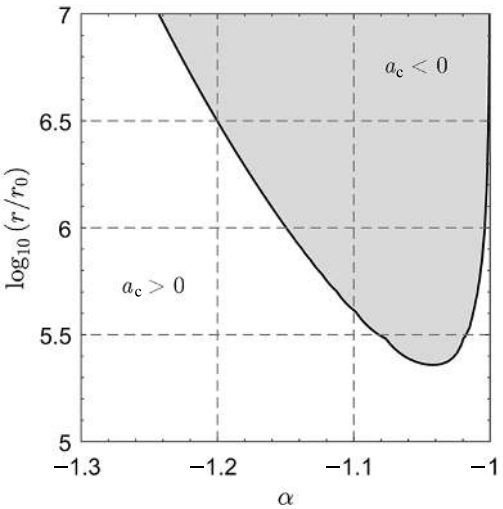

Fig. 6 Sign of a_c as a function of $\{\alpha, r\}$ for $a_{c_0} = 0$ and $e_0 = e_\oplus$.

Note that $a_c < 0$ occurs when r is several orders of magnitude greater than r_0. Thus, the required characteristic acceleration is in practise always non-negative,

especially when small values of e_0 are handled. For example, when $e_0 = e_\oplus$, the minimum value of r that would yield a negative a_c is more than 5 orders or magnitude greater than r_0, and it occurs when $\alpha \simeq -1.04$; see Fig. 6.

3.2 Required sail performance

Having found the conditions under which the generalized sail is able to provide an outward radial propulsive acceleration, the maximum required characteristic acceleration can now be determined. First, it is necessary to find the values of $\{\alpha, \gamma\}$ such that a_c is upper limited, that is, it converges to a finite value as $r \to +\infty$. To that end, since no propellantless propulsion systems are known with $\gamma > 2$, assume that $\gamma \leqslant 2$. In this case, the sum of the second and third term in the right-hand side of Eq. (40) reaches zero as $r \to +\infty$ when $\gamma < 2$, while it tends to $\mu_\odot / r_\oplus^2$ as $r \to +\infty$ when $\gamma = 2$. Therefore, bearing in mind Eq. (40), the required characteristic acceleration is upper limited as long as

$$\frac{2 + 3\alpha - \alpha\gamma}{\alpha} \geqslant 0 \tag{52}$$

Figure 7 shows the limits of a_c as $r \to +\infty$ for $\alpha \in [-2, 2]$ and $\gamma \in [0, 2]$. When $\{\alpha, \gamma\}$ belong to the grey areas in Fig. 7, the inequality (52) is met and the required propulsive acceleration tends to zero. In particular, when the limit is 0^-, the required characteristic acceleration first reaches a positive global maximum, then a negative global minimum and finally tends to zero. Instead, when the limit is 0^+, a_c simply reaches the global maximum before decreasing to zero without ever having negative values. In the white region, a_c reaches a positive global maximum and then it decreases indefinitely. Note that Fig. 7 confirms what was shown in the previous section about the sign of a_c. In fact, when $\alpha < -1$, a_c actually reaches negative values, even if this occurs when r is several orders of magnitude greater than r_0. Finally, in the hatched area $a_c \to +\infty$. It is worth noting that the hatched area is crossed by a dotted line. When $\{\alpha, \gamma\}$ lie below the dotted line, the required propulsive acceleration first reaches a local maximum, then a local minimum and finally tends to $+\infty$. Instead, when $\{\alpha, \gamma\}$ lie above the dotted line, a_c is a monotonic increasing function of r. For example, when $\alpha = -1/2$, a_c has both a local maximum and a local minimum as long as $\gamma \leqslant 1.6350$. Moreover, when $\gamma = \{0, 1, 4/3\}$, a_c becomes a monotonic increasing function of r when $\alpha > \{-0.2395, -0.3361, -0.4000\}$, respectively.

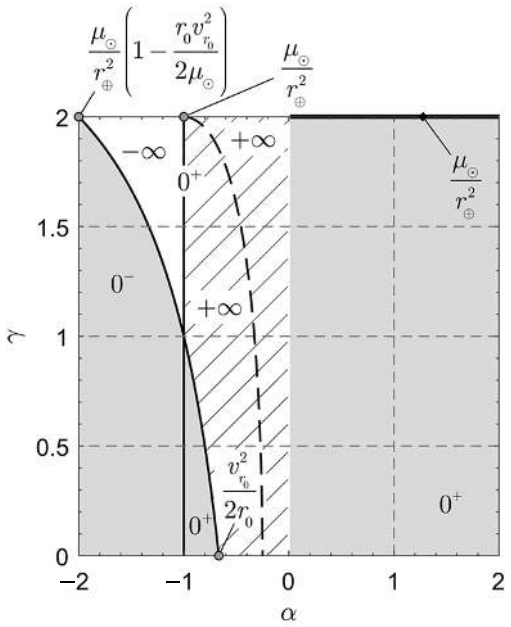

Fig. 7 Limit of a_c as $r \to +\infty$ as a function of $\{\alpha, \gamma\}$.

The solid black line that delimits the gray region in the lower left part of Fig. 7 is described by the equation $\gamma = 3 + 2/\alpha$ with $\alpha \in [-2, -2/3]$. If $\{\alpha, \gamma\}$ belong to that locus, then the required value of the characteristic acceleration becomes

$$a_c = -\frac{(1+\alpha) v_{r_0}^2 r_0^{\frac{2+2\alpha}{\alpha}}}{\alpha r_\oplus^{\frac{2+3\alpha}{\alpha}}} + \frac{\mu_\odot}{r_\oplus^{\frac{2+3\alpha}{\alpha}} r^{-\frac{2+\alpha}{\alpha}}} \left(1 - \frac{p_0}{r}\right) \tag{53}$$

from which

$$\lim_{r \to +\infty} a_c = \begin{cases} \dfrac{\mu_\odot}{r_\oplus^2}\left(1 - \dfrac{r_0 v_{r_0}^2}{2\mu_\odot}\right), & \text{if } \alpha = -2 \\ -\dfrac{(1+\alpha) v_{r_0}^2 r_0^{\frac{2+2\alpha}{\alpha}}}{\alpha r_\oplus^{\frac{2+3\alpha}{\alpha}}}, & \text{if } \alpha \in (-2, -2/3) \\ \dfrac{v_{r_0}^2}{2r_0}, & \text{if } \alpha = -2/3 \end{cases} \tag{54}$$

In particular, the sign of the second expression in the right-hand side of Eq. (54) is

$$\begin{cases} -\dfrac{(1+\alpha) v_{r_0}^2 r_0^{\frac{2+2\alpha}{\alpha}}}{\alpha r_\oplus^{\frac{2+3\alpha}{\alpha}}} < 0, & \text{if } \alpha \in (-2, -1) \\ -\dfrac{(1+\alpha) v_{r_0}^2 r_0^{\frac{2+2\alpha}{\alpha}}}{\alpha r_\oplus^{\frac{2+3\alpha}{\alpha}}} = 0, & \text{if } \alpha = -1 \\ -\dfrac{(1+\alpha) v_{r_0}^2 r_0^{\frac{2+2\alpha}{\alpha}}}{\alpha r_\oplus^{\frac{2+3\alpha}{\alpha}}} > 0, & \text{if } \alpha \in (-1, -2/3) \end{cases} \tag{55}$$

Another special case occurs when $\gamma = 2$ and the required characteristic acceleration becomes

$$a_{\mathrm{c}} = -\frac{(1+\alpha)v_{r_0}^2 r_0^{\frac{2+2\alpha}{\alpha}}}{\alpha r_{\oplus}^2 r^{\frac{2+\alpha}{\alpha}}} + \frac{\mu_{\odot}}{r_{\oplus}^2}\left(1 - \frac{p_0}{r}\right) \tag{56}$$

from which

$$\lim_{r\to+\infty} a_{\mathrm{c}} = \begin{cases} \dfrac{\mu_{\odot}}{r_{\oplus}^2}\left(1 - \dfrac{r_0 v_{r_0}^2}{2\mu_{\odot}}\right), & \text{if } \alpha = -2 \\ -\infty, & \text{if } \alpha \in (-2,-1) \\ \dfrac{\mu_{\odot}}{r_{\oplus}^2}, & \text{if } \alpha = -1 \\ +\infty, & \text{if } \alpha \in (-1,0) \\ \dfrac{\mu_{\odot}}{r_{\oplus}^2}, & \text{if } \alpha \in (0,2] \end{cases} \tag{57}$$

Finally, note that the hatched and the white areas are separated from each other by the vertical line of equation $\alpha = -1$, where $a_{\mathrm{c}} \to 0^+$. In this case, which is consistent with a hyperbolic spiral, Eq. (40) reduces to

$$a_{\mathrm{c}} = \frac{\mu_{\odot}}{r_{\oplus}^{\gamma} r^{2-\gamma}}\left(1 - \frac{p_0}{r}\right) \tag{58}$$

which is non-negative as long as $r_0 \geqslant p_0$.

The stationary points of a_{c} may be computed (provided that they exist) as a function of $\{\alpha, \gamma\}$ by solving the equation $\partial a_{\mathrm{c}}/\partial r = 0$ for a given value of ν_0. Assuming $\nu_0 = \widetilde{\nu}_0$ (i.e., when $v_{\theta_0} = \widetilde{v}_{\theta_0}$), the result is

$$\frac{(1+\alpha)v_{r_0}^2 r_0}{\alpha\mu_{\odot}}\left[\gamma - 3 + \frac{3\alpha - \alpha\gamma + 2}{\alpha}\left(\frac{r_0}{r}\right)^{2/\alpha}\right] + (\gamma - 2)\frac{r}{r_0} - \gamma + 3 = 0 \tag{59}$$

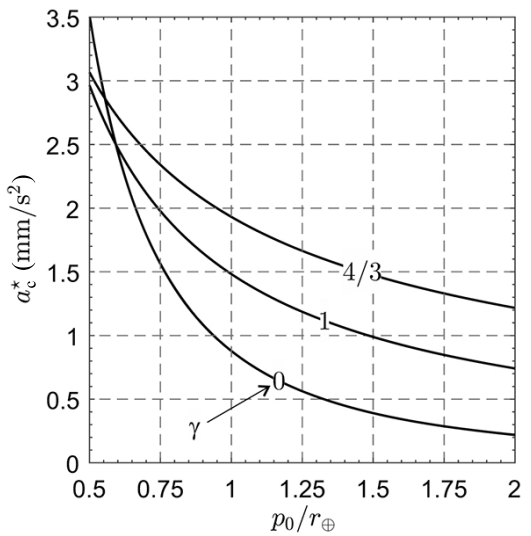

Fig. 8 Maximum value of $a_{\mathrm{c}}^{\star}$ as a function of $\{p_0, \gamma\}$ for a hyperbolic spiral ($\alpha = -1$).

Equation (59) admits an analytical solution when $\alpha = \{-2, -1, 2\}$. In those special cases the result is

$$r^{\star} = \begin{cases} \dfrac{(3-\gamma)r_0}{2-\gamma}, & \text{if } \alpha = \{-2,-1\} \\ \dfrac{\left[\begin{array}{l}(3-\gamma)(1-\beta)+ \\ \sqrt{(3-\gamma)^2(1-\beta)^2 + 4(2-\gamma)(4-\gamma)\beta}\end{array}\right] r_0}{2(2-\gamma)}, & \text{if } \alpha = 2 \end{cases} \tag{60}$$

where

$$\beta \triangleq \frac{3v_{r_0}^2 r_0}{2\mu_{\odot}} \tag{61}$$

It is worth noting that the equation $\partial a_{\mathrm{c}}/\partial r = 0$ can also be analytically solved when $\alpha = -1$ (see Eq. (58)) for any value of ν_0. In this case, the necessary condition for a maximum (i.e., $\partial a_{\mathrm{c}}/\partial r = 0$) provides

$$r^{\star} = \frac{(3-\gamma)p_0}{2-\gamma} \tag{62}$$

which is valid as long as $\gamma < 2$ because $r^{\star}$ must also satisfy the constraint $r^{\star} \geqslant p_0$. Substituting Eq. (62) into Eq. (58), the maximum value of a_{c} is given by

$$a_{\mathrm{c}}(r^{\star}) = a_{\mathrm{c}}^{\star} \triangleq \frac{\mu_{\odot}}{r_{\oplus}^{\gamma} p_0^{2-\gamma}} \frac{(2-\gamma)^{2-\gamma}}{(3-\gamma)^{3-\gamma}} \tag{63}$$

Figure 8 shows the maximum value of the required characteristic acceleration as a function of $\{p_0, \gamma\}$ when $\alpha = -1$. It is worth noting that $a_{\mathrm{c}}^{\star}$ decreases as p_0 increases.

4 Case study

Consider a generalized sail-based spacecraft that leaves the Earth's sphere of influence on a parabolic escape trajectory. Assume that the sail deployment occurs when the true anomaly on the heliocentric parking orbit (which therefore coincides with the Earth's orbit) is $\nu_0 = \widetilde{\nu}_0$; see Eq. (48). In this scenario, the variation of $\widetilde{\nu}_0$ with α is shown in Fig. 9 for $\alpha \in [-2, 2]$, illustrating that, owing to the small Earth's orbit eccentricity, the value of $\widetilde{\nu}_0$ is very close to $\pi/2$ rad when $|\alpha| \in [1/2, 1]$.

The ratios $r^{\star}/r_0$ that solve Eq. (59) are represented in Fig. 10 for $\alpha \in [-1, 1]$, $\gamma = \{0, 4/3, 1, 1.635\}$, and $e_0 = e_{\oplus}$.

Note that, when $\alpha \in (-0.2395, 0)$, no stationary point exists for all the considered values of γ, which implies that a_{c} always increases with r in that range; see also Fig. 7.

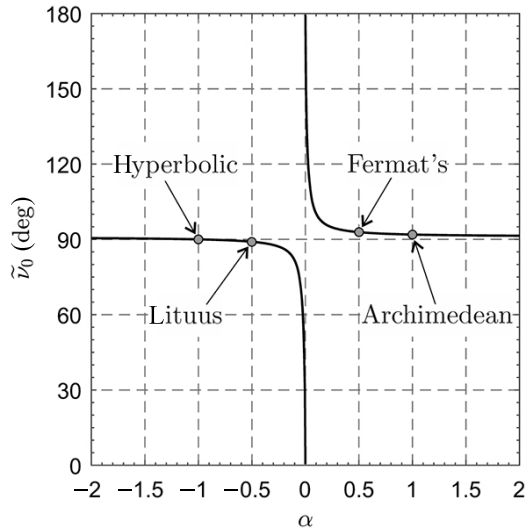

Fig. 9 Variation of $\widetilde{\nu}_0$ with α when $e_0 = e_\oplus$.

Moreover, consistently with Fig. 7, Fig. 10 shows that a_c actually has two stationary points (that is, a positive local maximum and a positive local minimum) before going to $+\infty$ when $\alpha \in (-1, -0.2395)$. It is also worth noting that the second stationary point (i.e., the positive local minimum) is much greater than the first one (i.e., the positive local maximum) when $\alpha \in (-1, -1/2]$ and $\gamma = \{0, 1, 4/3\}$. This implies that the required characteristic acceleration becomes greater than its local maximum after a such large time interval that, basically, the local maximum may be used as a design parameter of the generalized sail.

Figure 10 shows that the dimensionless distance $r^\star/r_0$, at which a local maximum occurs, is nearly independent of α when $\gamma = \{0, 4/3, 1\}$ and $\alpha \leqslant -1/2$ or $\alpha > 0$. This implies that, in those cases, the maximum required characteristic acceleration is substantially independent of the type of spiral that the spacecraft is travelling, but only depends on the specific propulsion system. Therefore, Eq. (63) may be used to estimate $a_c^\star$ when $\alpha \neq -1$.

In the presented case study, $p_0 = p_\oplus \simeq 0.9997208$ au and $e_0 = e_\oplus$. Accordingly, Eq. (63) provides

$$\begin{cases} a_c^\star \simeq 0.8790 \text{ mm/s}^2, & \text{if } \gamma = 0 \\ a_c^\star \simeq 1.4829 \text{ mm/s}^2, & \text{if } \gamma = 1 \\ a_c^\star \simeq 1.9320 \text{ mm/s}^2, & \text{if } \gamma = 4/3 \end{cases} \tag{64}$$

Figures 11–14 show the trajectories and the required characteristic accelerations as a function of $\alpha = \{-1, -1/2, 1/2, 1\}$, when $p_0 = p_\oplus$, $e_0 = e_\oplus$, and $\nu_0 = \widetilde{\nu}_0$. In all cases, as expected, $a_{c_0} = 0$. By comparing Figs. 11(a), 12(a), 13(a), and 14(a), it is worth noting that the orbital radius grows faster when $\alpha = -1/2$, that is, when the spacecraft travels a lituus. Instead, the slowest growth of r occurs when $\alpha = 1/2$, that is, when the spacecraft travels a Fermat's spiral. In fact, after a 20 year-long journey, the spacecraft orbital radius is approximately equal to 8.1684 au when $\alpha = -1/2$, while it is only 1.7512 au when $\alpha = 1/2$. However, note that the orbital radius grows even faster if $\alpha \in (-1/2, 0)$. In fact, comparing Eqs. (15) and (26) it may be verified that, when $\alpha \in (-1/2, 0)$:

$$\chi^{\frac{\alpha}{1+2\alpha}} > \exp\left(\frac{v_{r_0} t}{r_0}\right) \tag{65}$$

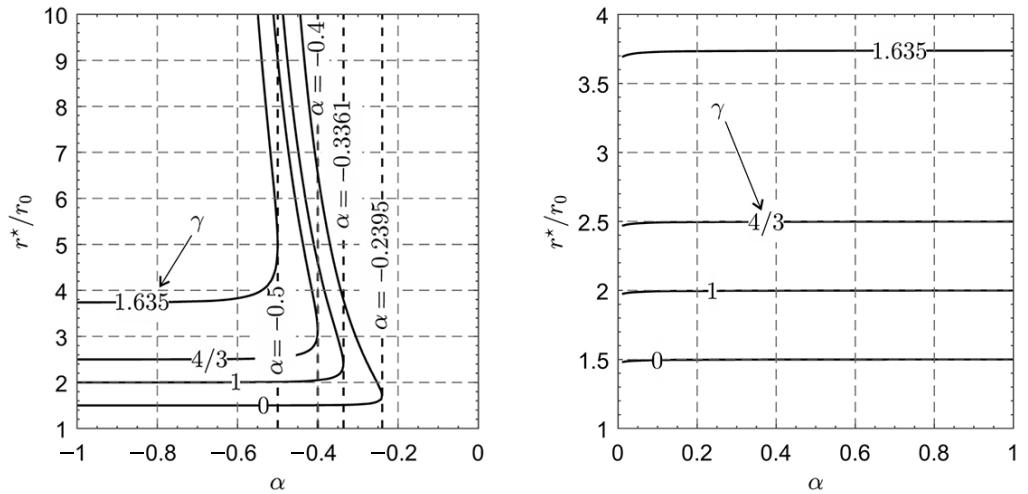

(a) $\alpha < 0$ (b) $\alpha > 0$

Fig. 10 Ratio $r^\star/r_0$ that solves Eq. (59) as a function of $\{\alpha, \gamma\}$ for $a_{c_0} = 0$ and $e_0 = e_\oplus$.

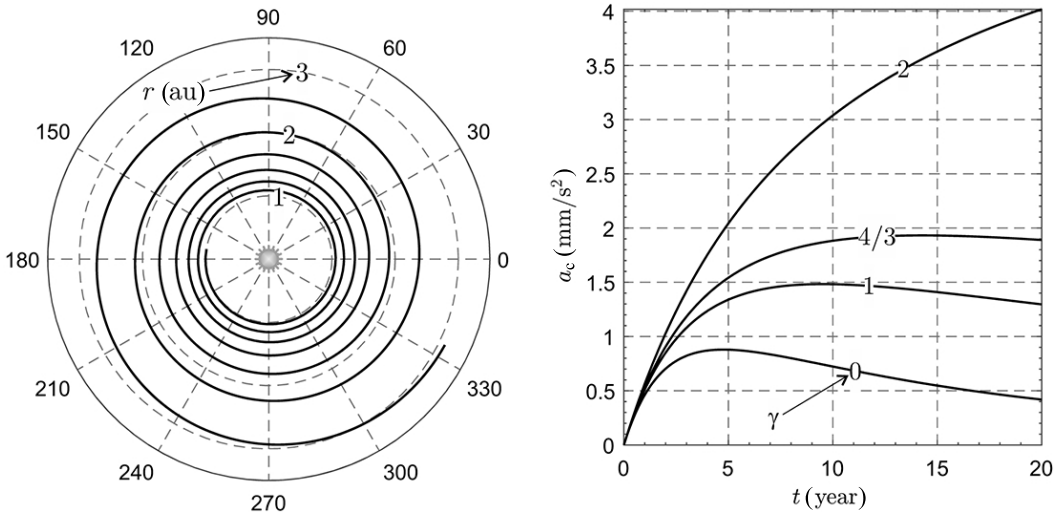

(a) Hyperbolic spiral trajectory from Earth's orbit assuming $\nu_0 = \widetilde{\nu}_0 = 90$ deg.

(b) Required a_c as a function of $\{t, \gamma\}$.

Fig. 11 Generalized sail-based hyperbolic spiral.

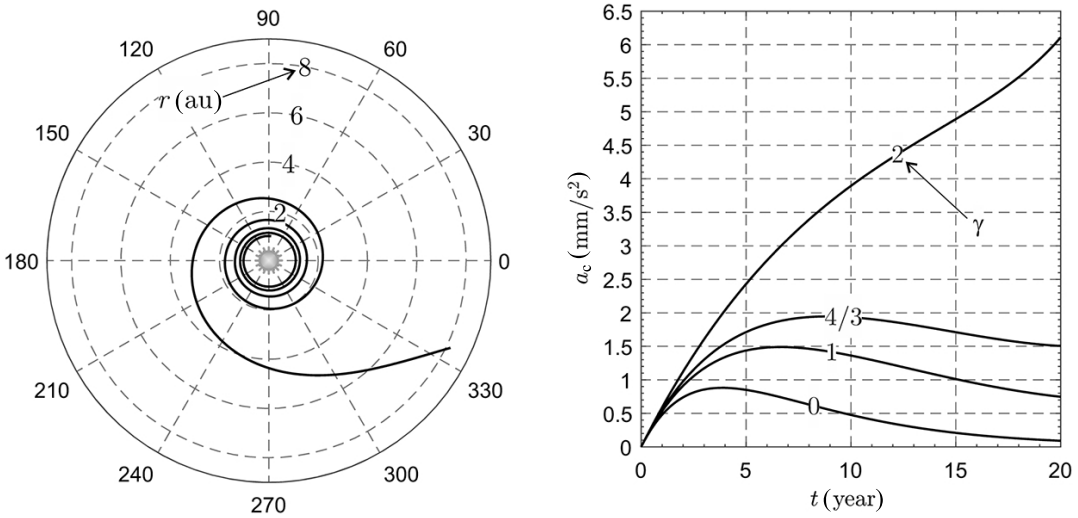

(a) Lituus trajectory from Earth's orbit assuming $\nu_0 = \widetilde{\nu}_0 \simeq 89.04$ deg.

(b) Required a_c as a function of $\{t, \gamma\}$.

Fig. 12 Generalized sail-based lituus.

for all $t \in (0, t_{\max})$; see Eq. (17). Finally, Figs. 11(b), 12(b), 13(b), and 14(b) confirm that the maximum value of a_c essentially depends on γ only and prove that Eq. (63) (which is exact when $\alpha = -1$) provides an accurate estimate of $a_c^\star$ when $\alpha \neq -1$.

5 Conclusions

In this study, new analytical solutions to the equations of motion of a radially propelled spacecraft have been investigated, with the starting hypothesis that the spacecraft orbital radius is proportional to a given power of its angular coordinate. The expressions of the spacecraft state variables and the orbital elements of the osculating orbit have been derived in exact form as a function of time, and the required propulsive acceleration necessary for the spacecraft to track the prescribed spiral trajectory has been calculated a posteriori.

The analytical results have been specialized to the case of a generalized sail, a propulsion system in which the magnitude scales with an assigned power of the Sun–spacecraft distance. The conditions for an outward radial

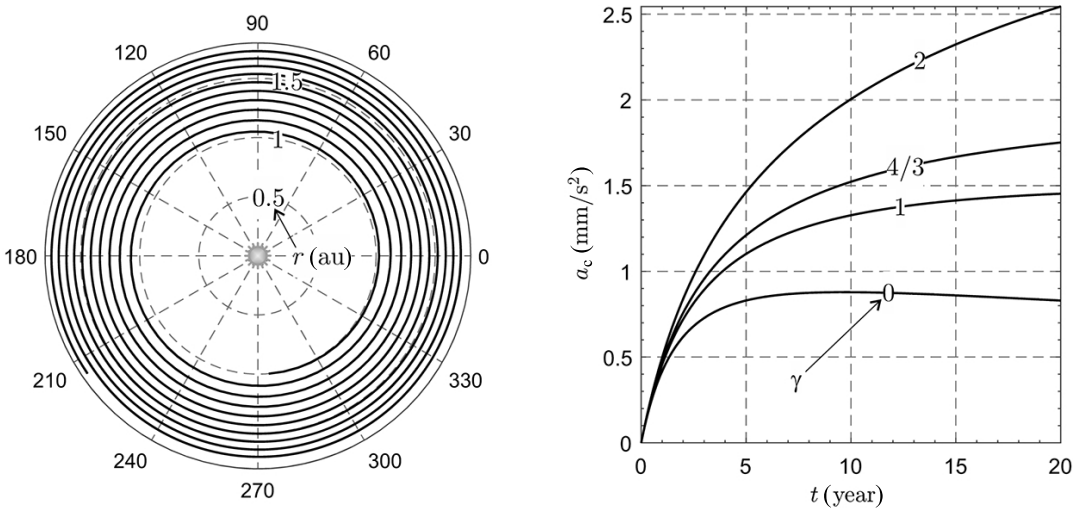

(a) Fermat's spiral trajectory from Earth's orbit assuming $\nu_0 = \widetilde{\nu}_0 \simeq 92.87$ deg.

(b) Required a_c as a function of $\{t, \gamma\}$.

Fig. 13 Generalized sail-based Fermat's spiral.

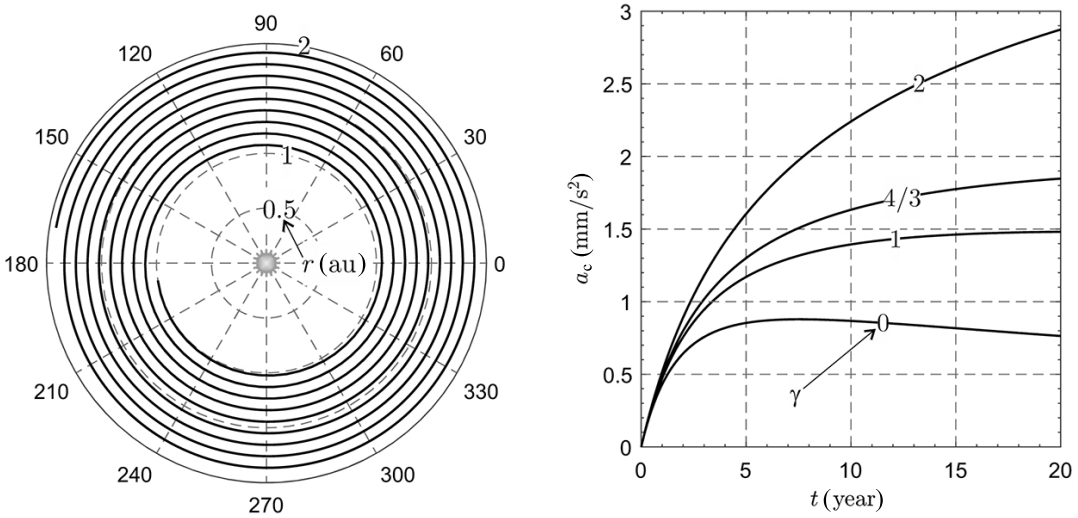

(a) Archimedean spiral trajectory from Earth's orbit assuming $\nu_0 = \widetilde{\nu}_0 \simeq 91.91$ deg.

(b) Required a_c as a function of $\{t, \gamma\}$.

Fig. 14 Generalized sail-based Archimedean spiral.

thrust and the required sail performance have been quantified and thoroughly discussed, demonstrating that the maximum required characteristic acceleration (a sail performance parameter) is substantially independent of the type of spiral, but it only depends on the features of the specific propulsion system. Moreover, an analytical approximation of the maximum required characteristic acceleration has been proposed, which is valid for any spiral and any type of generalized sail.

A case study has finally been presented, in which the spacecraft parking orbit coincides with the Earth's heliocentric orbit. In particular, it has been shown that the maximum required characteristic acceleration is on the order of one millimeter per second squared when the spacecraft travels some reference spiral trajectories, a feasible value on the basis of many results available in the literature.

Funding note

Open Access funding provided by University of Pisa within the CRUICARE Agreement.

References

[1] Markopoulos, N. Analytically exact non-Keplerian motion for orbital transfers. In: Proceedings of the Astrodynamics Conference, **1994**: AIAA-94-3758-CP.

[2] Petropoulos, A. E., Sims, J. A. A review of some exact solutions to the planar equations of motion of a thrusting spacecraft anastassios. *International Symposium Low Thrust Trajectories*, **2002**, 2(1): 1–14.

[3] McInnes, C. R. Orbits in a generalized two-body problem. *Journal of Guidance, Control, and Dynamics*, **2003**, 26(5): 743–749.

[4] Tsien, H. S. Take-off from satellite orbit. *Journal of the American Rocket Society*, **1953**, 23(4): 233–236.

[5] Prussing, J. E., Coverstone-Carroll, V. Constant radial thrust acceleration redux. *Journal of Guidance, Control, and Dynamics*, **1998**, 21(3): 516–518.

[6] Mengali, G., Quarta, A. A. Escape from elliptic orbit using constant radial thrust. *Journal of Guidance, Control, and Dynamics*, **2009**, 32(3): 1018–1022.

[7] Battin, R. H. *An Introduction to the Mathematics and Methods of Astrodynamics*. New York: AIAA, Inc., **1999**: 408–415.

[8] Quarta, A. A., Mengali, G. New look to the constant radial acceleration problem. *Journal of Guidance, Control, and Dynamics*, **2012**, 35(3): 919–929.

[9] Gonzalo, J. L., Bombardelli, C. Asymptotic solution for the two body problem with radial perturbing acceleration. In: Proceedings of the 24th AAS/AIAA Space Flight Mechanics Meeting, **2014**.

[10] Izzo, D., Biscani, F. Explicit solution to the constant radial acceleration problem. *Journal of Guidance, Control, and Dynamics*, **2015**, 38(4): 733–739.

[11] Quarta, A. A., Mengali, G. Analysis of spacecraft motion under constant circumferential propulsive acceleration. *Acta Astronautica*, **2014**, 105(1): 278–284.

[12] Niccolai, L., Quarta, A. A., Mengali, G. Orbital motion approximation with constant circumferential acceleration. *Journal of Guidance, Control, and Dynamics*, **2018**, 41(8): 1783–1789.

[13] Bombardelli, C., Baù, G., Peláez, J. Asymptotic solution for the two-body problem with constant tangential thrust acceleration. *Celestial Mechanics and Dynamical Astronomy*, **2011**, 110(3): 239–256.

[14] Quarta, A. A., Mengali, G., Caruso, A. Optimal circle-to-rectilinear orbit transfer with circumferential thrust. *Astrodynamics*, **2019**, 3(1): 31–43.

[15] Benney, D. J. Escape from a circular orbit using tangential thrust. *Journal of Jet Propulsion*, **1958**, 28(3): 167–169.

[16] Boltz, F. W. Orbital motion under continuous tangential thrust. *Journal of Guidance, Control, and Dynamics*, **1992**, 15(6): 1503–1507.

[17] Roa, J., Peláez, J., Senent, J. New analytic solution with continuous thrust: Generalized logarithmic spirals. *Journal of Guidance, Control, and Dynamics*, **2016**, 39(10): 2336–2351.

[18] Bacon, R. H. Logarithmic spiral: An ideal trajectory for the interplanetary vehicle with engines of low sustained thrust. *American Journal of Physics*, **1959**, 27(3): 164–165.

[19] Tsu, T. C. Interplanetary travel by solar sail. *ARS Journal*, **1959**, 29(6): 422–427.

[20] McInnes, C. R. *Solar Sailing: Technology, Dynamics and Mission Applications*. Berlin: Springer-Verlag, **1999**.

[21] Fu, B., Sperber, E., Eke, F. Solar sail technology—A state of the art review. *Progress in Aerospace Sciences*, **2016**, 86: 1–19.

[22] Gong, S. P., MacDonald, M. Review on solar sail technology. *Astrodynamics*, **2019**, 3(2): 93–125.

[23] Bassetto, M., Niccolai, L., Quarta, A. A., Mengali, G. Logarithmic spiral trajectories generated by Solar sails. *Celestial Mechanics and Dynamical Astronomy*, **2018**, 130(2): 18.

[24] Petropoulos, A. E., Longuski, J. M. Shape-based algorithm for the automated design of low-thrust, gravity assist trajectories. *Journal of Spacecraft and Rockets*, **2004**, 41(5): 787–796.

[25] Izzo, D. Lambert's problem for exponential sinusoids. *Journal of Guidance, Control, and Dynamics*, **2006**, 29(5): 1242–1245.

[26] Wall, B. J., Conway, B. A. Shape-based approach to low-thrust rendezvous trajectory design. *Journal of Guidance, Control, and Dynamics*, **2009**, 32(1): 95–101.

[27] Taheri, E., Abdelkhalik, O. Shape-based approximation of constrained low-thrust space trajectories using Fourier series. *Journal of Spacecraft and Rockets*, **2012**, 49(3): 535–545.

[28] Taheri, E., Abdelkhalik, O. Fast initial trajectory design for low-thrust restricted-three-body problems. *Journal of Guidance, Control, and Dynamics*, **2015**, 38(11): 2146–2160.

[29] Taheri, E., Abdelkhalik, O. Initial three-dimensional low-thrust trajectory design. *Advances in Space Research*, **2016**, 57(3): 889–903.

[30] Aliasi, G., Mengali, G., Quarta, A. A. Artificial equilibrium points for a generalized sail in the circular restricted three-body problem. *Celestial Mechanics and Dynamical Astronomy*, **2011**, 110(4): 343–368.

[31] Aliasi, G., Mengali, G., Quarta, A. A. Artificial equilibrium points for a generalized sail in the elliptic restricted three-body problem. *Celestial Mechanics and Dynamical Astronomy*, **2012**, 114(1–2): 181–200.

[32] Aliasi, G., Mengali, G., Quarta, A. A. Artificial periodic orbits around L1-type equilibrium points for a generalized sail. *Journal of Guidance, Control, and Dynamics*, **2015**, 38(9): 1847–1852.

[33] Janhunen, P. Electric sail for spacecraft propulsion. *Journal of Propulsion and Power*, **2004**, 20(4): 763–764.

[34] Janhunen, P., Sandroos, A. Simulation study of solar wind push on a charged wire: Basis of solar wind electric sail propulsion. *Annales Geophysicae*, **2007**, 25(3): 755–767.

[35] Mengali, G., Quarta, A. A., Janhunen, P. Electric sail performance analysis. *Journal of Spacecraft and Rockets*, **2008**, 45(1): 122–129.

[36] Janhunen, P., Toivanen, P. K., Polkko, J., Merikallio, S., Salminen, P., Haeggström, E., Seppänen, H., Kurppa, R., Ukkonen, J., Kiprich, S. *et al.* Invited article: Electric solar wind sail: Toward test missions. *The Review of Scientific Instruments*, **2010**, 81(11): 111301.

[37] Janhunen, P. Status report of the electric sail in 2009. *Acta Astronautica*, **2011**, 68(5–6): 567–570.

[38] Andrews, D., Zubrin, R. Use of magnetic sails for Mars exploration missions. In: Proceedings of the 25th Joint Propulsion Conference, **1989**: AAAA-89-2861.

[39] Andrews, D. G., Zubrin, R. M. Progress in magnetic sails. In: Proceedings of the AIAA/ASME/SAE/ASEE 26th Joint Propulsion Conference, **1990**.

[40] Andrews, D. G., Zubrin, R. M. Magnetic sails and interstellar travel. *Journal of the British Interplanetary Society*, **1990**, 43(6): 265–272.

[41] Zubrin, R. M., Andrews, D. G. Magnetic sails and interplanetary travel. *Journal of Spacecraft and Rockets*, **1991**, 28(2): 197–203.

[42] Zubrin, R. The use of magnetic sails to escape from low earth orbit. In: Proceedings of the 27th Joint Propulsion Conference, **1991**: AIAA-91-3352.

[43] Niccolai, L., Bassetto, M., Quarta, A. A., Mengali, G. A review of smart dust architecture, dynamics, and mission applications. *Progress in Aerospace Sciences*, **2019**, 106: 1–14.

[44] Quarta, A. A., Mengali, G., Niccolai, L. Smart dust option for geomagnetic tail exploration. *Astrodynamics*, **2019**, 3(3): 217–230.

[45] Bassetto, M., Mengali, G., Quarta, A. A. Stability and control of spinning electric solar wind sail in heliostationary orbit. *Journal of Guidance, Control, and Dynamics*, **2019**, 42(2): 425–431.

[46] Atchison, J. A., Peck, M. A. A passive, Sun-pointing, millimeter-scale solar sail. *Acta Astronautica*, **2010**, 67(1–2): 108–121.

[47] Quarta, A. A., Mengali, G. Trajectory approximation for low-performance electric sail with constant thrust angle. *Journal of Guidance, Control, and Dynamics*, **2013**, 36(3): 884–887.

[48] Quarta, A. A., Mengali, G. Analysis of electric sail heliocentric motion under radial thrust. *Journal of Guidance, Control, and Dynamics*, **2016**, 39(6): 1433–1437.

[49] Niccolai, L., Quarta, A. A., Mengali, G. Two-dimensional heliocentric dynamics approximation of an electric sail with fixed attitude. *Aerospace Science and Technology*, **2017**, 71: 441–446.

[50] Quarta, A. A., Mengali, G. Approximate solutions to circle-to-circle solar sail orbit transfer. *Journal of Guidance, Control, and Dynamics*, **2013**, 36(6): 1886–1890.

[51] Niccolai, L., Quarta, A. A., Mengali, G. Solar sail trajectory analysis with asymptotic expansion method. *Aerospace Science and Technology*, **2017**, 68: 431–440.

[52] Caruso, A., Bassetto, M., Mengali, G., Quarta, A. A. Optimal solar sail trajectory approximation with finite Fourier series. *Advances in Space Research*, **2019**, https://doi.org/10.1016/j.asr.2019.11.019.

[53] Biggs, J. D., McInnes, C. R. Passive orbit control for space-based geo-eEngineering. *Journal of Guidance, Control, and Dynamics*, **2010**, 33(3): 1017–1020.

[54] Aliasi, G., Mengali, G., Quarta, A. A. Artificial Lagrange points for solar sail with electrochromic material panels. *Journal of Guidance, Control, and Dynamics*, **2013**, 36(5): 1544–1550.

[55] Huo, M. Y., Mengali, G., Quarta, A. A. Electric sail thrust model from a geometrical perspective. *Journal of Guidance Control and Dynamics*, **2017**, 41(3): 735–741.

[56] Quarta, A. A., Mengali, G., Aliasi, G. Optimal control laws for heliocentric transfers with a magnetic sail. *Acta Astronautica*, **2013**, 89: 216–225.

[57] Bassetto, M., Quarta, A. A., Mengali, G. Magnetic sail-based displaced non-Keplerian orbits. *Aerospace Science and Technology*, **2019**, 92: 363–372.

Marco Bassetto graduated in aerospace engineering at the University of Pisa in 2016. In 2019, he received his Ph.D. degree in civil and industrial engineering at the Department of Civil and Industrial Engineering of the University of Pisa. He currently holds a post-doc scholarship in the same department. His research activity focuses on trajectory design and attitude control of

spacecraft propelled with low-thrust propulsion systems such as solar sails and electric solar wind sails. E-mail: marco.bassetto@ing.unipi.it.

Alessandro A. Quarta received his Ph.D. degree in aerospace engineering from the University of Pisa in 2005, and is currently a professor of flight mechanics at the Department of Civil and Industrial Engineering of the University of Pisa. His main research areas include spaceflight simulation, spacecraft mission analysis and design, low-thrust trajectory optimization, solar sail, and E-sail dynamics and control. E-mail: a.quarta@ing.unipi.it.

Giovanni Mengali received his doctor of engineering degree in aeronautical engineering in 1989 from the University of Pisa. Since 1990, he has been with the Department of Aerospace Engineering (now Department of Civil and Industrial Engineering) of the University of Pisa, first as a Ph.D. student, then as an assistant and an associate professor. Currently, he is a professor of spaceflight mechanics. His main research areas include spacecraft mission analysis, trajectory optimization, solar sails, electric sails, and aircraft flight dynamics and control. E-mail: g.mengali@ing.unipi.it.

Vittorio Cipolla received his Ph.D. degree discussing a thesis on high altitude-long endurance UAVs powered by solar energy. Between 2011 and 2019 he has participated in several research projects, including "PARSIFAL" (PrandtlPlane Architecture for the Sustainable Improvement of Future Airplanes) and "PROSIB" (hybrid propulsion systems for fixed and rotary wing aircraft). Since 2018 he is a research fellow at the University of Pisa, where he also teaches applied aeroelasticity in M.Sc. course of aerospace engineering. E-mail: vittorio.cipolla@unipi.it.